

Mid-infrared spectroscopy of the Andromeda galaxy

D. Hemachandra^{1*}, P. Barmby¹, E. Peeters^{1,2}, S.P. Willner³, M.L.N. Ashby³, H.A. Smith³, K.D. Gordon⁴, D.A. Smith⁴, and G.G. Fazio³

¹*Department of Physics and Astronomy, University of Western Ontario, London, ON, N6A 3K7, Canada*

²*SETI Institute, 189 Bernardo Avenue, Suite 100, Mountain View, CA 94043, USA*

³*Harvard-Smithsonian Center for Astrophysics, Cambridge, MA 02138, USA*

⁴*Space Telescope Science Institute, 3700 San Martin Drive, Baltimore, MD 21218, USA*

ABSTRACT

We present *Spitzer*/Infrared Spectrograph 5–21 μm spectroscopic maps towards 12 regions in the Andromeda galaxy (M31). These regions include the nucleus, bulge, an active region in the star-forming ring, and 9 other regions chosen to cover a range of mid-to-far-infrared colours. PAH feature ratios (6.2 μm and 7.7 μm features compared to the 11.3 μm feature) measured from our extracted M31 spectra are consistent with those seen in other nearby galaxies. Our observations did not reproduce the suppressed 6–8 μm features and enhanced 11.3 μm feature seen with the ISOCAM instrument on the Infrared Space Observatory. The equivalent widths of the main PAH features decrease with increasing radiation hardness, consistent with that observed for other nearby spiral and starburst galaxies. The nucleus does not show any PAH emission except for the 11.3 μm feature but does show strong silicate emission at 9.7 μm . Both of these characteristics provide evidence for a low luminosity active galactic nucleus in M31.

Key words: galaxies: individual: M31 – galaxies: ISM – galaxies: nuclei – infrared: ISM – ISM: molecules – ISM: lines and bands

1 INTRODUCTION

Mid-infrared spectra provide a unique diagnostic tool to understand the physical conditions in the interstellar medium of galaxies. The rich range of spectral features (Polycyclic Aromatic Hydrocarbons (PAHs), atomic fine structure lines (e.g. Ne, S) and the amorphous silicate feature centred at 9.7 μm) provide information on dust properties, radiation field and star formation. With the advent of infrared space telescopes, such as the Infrared Space Observatory (ISO, Kessler et al. 1996) and the *Spitzer* Space Telescope (Werner et al. 2004), mid-infrared spectroscopy has become an important method of investigating the infrared emission from galaxies.

PAHs are known as the main carrier of the ubiquitous mid-infrared emission bands (e.g. Allamandola et al. 1989, Puget & Leger 1989). They are large hydrocarbon molecules consisting of ~ 50 –100 carbon atoms (Tielens 2008). The main PAH features are seen at 3.3, 6.2, 7.7, 8.6, 11.3 and 12.7 μm (e.g., Gillett et al. 1973, Geballe et al. 1985, Peeters 2011). These bands are attributed to the vibrational de-excitation of PAH molecules through bending and stretching modes of C-H and C-C bonds (e.g. Allamandola et al.

1989, Puget & Leger 1989). The 6 to 8 micron features are thought to originate mostly from ionized PAHs and the 3.3 and 11.3 μm emission bands from neutral PAHs (e.g. Hudgins & Allamandola 2004 and reference therein, Hony et al. 2001, Galliano et al. 2008a).

The relative strength of the PAH features vary spatially within extended objects and from galaxy-to-galaxy (e.g. Galliano et al. 2008a). While extinction does influence the individual PAH bands to different degrees (e.g. Brandl et al. 2006; Stock et al. 2013), the observed spread in PAH intensity ratios is dominated by the PAH charge balance (Galliano et al. 2008a). In addition, feature ratios do change more drastically close to active galactic nuclei where the overall strength of PAH emission also gets weaker (Roche et al. 1991, Smith et al. 2007b). Smith et al. (2007b) found that the mid-infrared spectra from some weak AGNs show suppressed 6 to 8 μm PAH features (by up to a factor of 10 in strength) but are bright at 11.3 μm . One possible explanation for this behaviour is that AGNs alter the grain composition by selective destruction of small PAHs and/or even can excite the PAHs. Alternatively, the PAH emission is modified by the low star formation intensity in the centers of many AGNs (Smith et al. 2007b).

Previous studies of nearby galaxies indicate that metallicity and radiation hardness can both affect the PAH emis-

* E-mail: dhemacha@uwo.ca

sion (e.g. Madden 2000, Beirão et al. 2006, Engelbracht et al. 2008, Muñoz-Mateos et al. 2009). In particular, the PAH equivalent widths (EQWs) in nearby galaxies decrease with increasing radiation hardness, although Brandl et al. (2006) found no such correlation within their starburst sample. In addition, PAH EQWs show an anti-correlation with metallicity in star-forming galaxies. This variation of PAHs among galaxies has also been observed within H II regions of M101 (Gordon et al. 2008). But there are no other investigations done on a single star-forming galaxy with sufficiently high resolution to see whether the correlations mentioned above hold within a galaxy similar to the Milky Way.

The amorphous silicate feature at $9.7\ \mu\text{m}$ is another aspect of the mid-infrared spectra of galaxies and in particular their nuclei. Spoon et al. (2007) classified infrared galaxies based on the equivalent width of the $6.2\ \mu\text{m}$ PAH feature and the strength of the $9.7\ \mu\text{m}$ silicate feature. They found galaxies spread along two distinct branches: one in which silicate absorption strength was anti-correlated with PAH equivalent width, and another in which the weak silicate feature strength did not depend on the $6.2\ \mu\text{m}$ equivalent width. Silicate emission at $9.7\ \mu\text{m}$ has also been observed in both Seyfert 1 and Seyfert 2 galaxies and can be used to constrain the geometry and structure of the emitting nuclear region (Mason et al. 2009).

M31 with its proximity ($785 \pm 25\ \text{kpc}$; McConnachie et al. 2005) and rich observational databases provides the most detailed view of a star forming galaxy similar to the Milky Way. The active star forming ring visible in $8\ \mu\text{m}$ *Spitzer*/IRAC images (Barmby et al. 2006) provides evidence of abundant PAHs in M31. However, ISOCAM spectro-imaging observations of M31 (Cesarsky et al. 1998) showed that four regions including the nucleus and bulge of this galaxy have very odd PAH spectra, bright at $11.3\ \mu\text{m}$ while showing weak or no 6.2 , 7.7 , and $8.6\ \mu\text{m}$ bands. Investigating this unusual PAH emission was the main motivation for the work described in this paper. The centre of M31 has a complicated physical structure. It hosts a very inactive supermassive black hole with a mass of $0.7 - 1.4 \times 10^8\ M_{\odot}$ (Bacon et al. 2001; Bender et al. 2005) and also has a lopsided nuclear disk with two stellar components (Lauer et al. 1993) and an A-star cluster (Bender et al. 2005). While M31's nucleus is known to be inactive from an X-ray perspective (Li et al. 2011), mid-infrared indicators of its nuclear activity, such as infrared excess or spectral features of silicates, have received relatively little attention. The higher spatial resolution available in observations of a very nearby galaxy like M31, compared to luminous, distant objects such as ultra-luminous infrared galaxies (Spoon et al. 2007) or nearby Seyferts (Mason et al. 2009), makes exploring its mid-infrared spectrum worthwhile.

We employed mid-infrared spectral maps from the *Spitzer*/Infrared Spectrograph (IRS) from 12 regions of M31 for a further investigation of its infrared properties. This sample includes the nucleus, bulge, an active region in the star-forming ring (all previously observed by ISOCAM), and 9 other regions chosen to cover a range of properties as described in Section 2.1. We obtained the processed version of ISOCAM observations of M31 and compare them with the IRS results in Section 3.1. Section 4.1 discusses PAH intensity ratios. In Section 4.2, we investigate the relationship between PAH equivalent widths and radiation hardness and



Figure 1. $8 - 24/70 - 160\ \mu\text{m}$ colour-colour diagram of M31 obtained from IRAC and MIPS imaging. Colour-coding of points represents $24\ \mu\text{m}$ flux, from faintest (blue) to brightest (red). The plot is divided into 9 regions (black grid), and the observations were made to cover those regions subject to a $24\ \mu\text{m}$ brightness cut. The black triangles indicate colours of the regions we observed.

compare to that found by Engelbracht et al. (2008) and Gordon et al. (2008). Metallicity and PAH EQWs are compared in Section 4.3, and Section 4.4 discusses the dust properties of the nucleus. The paper is summarized in Section ??.

2 OBSERVATIONS AND DATA REDUCTION

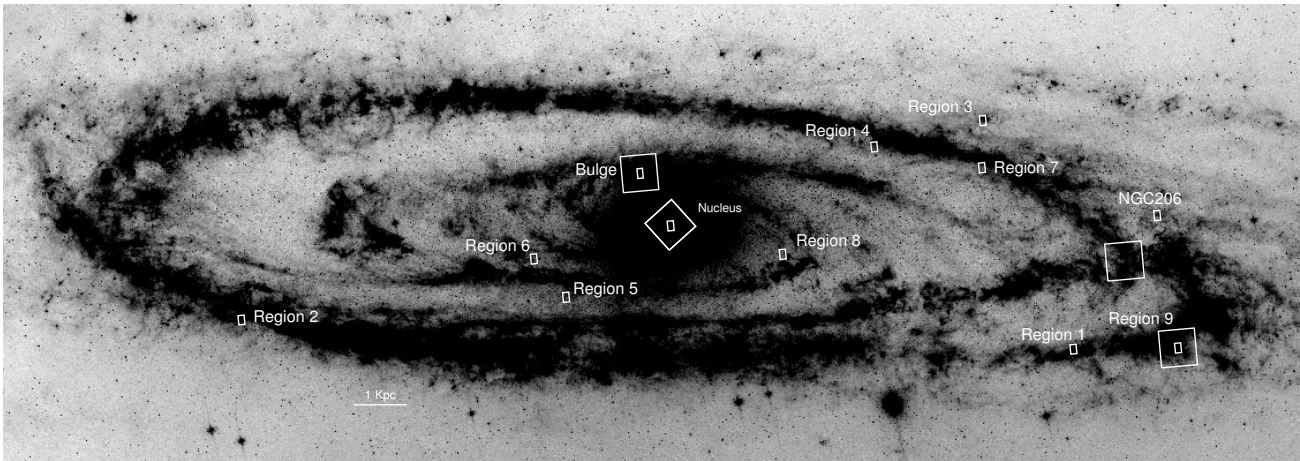
2.1 IRS observations

We obtained mid-infrared spectral maps of 12 regions in M31 using the *Spitzer*/IRS instrument (Houck et al. 2004) covering wavelengths from 5 to 21 microns. These regions include the nucleus, the ‘bulge’ and ‘active’ regions previously observed by ISOCAM (the latter is Region 9 in our sample), and 9 other regions chosen to cover a range of metallicities and dust temperatures. The 9 regions were chosen by convolving the IRAC $8\ \mu\text{m}$ (Barmby et al. 2006) and MIPS (Gordon et al. 2006) maps to the same resolution and constructing an $8 - 24/70 - 160\ \mu\text{m}$ colour-colour diagram (Figure 1). This colour space was used to give a rough definition of the types of spectral energy distribution; the dense region in the plot was split into a 3×3 grid and one pixel in each grid region (subject to a $24\ \mu\text{m}$ brightness cut) was selected for spectroscopy. The locations of the observed regions are shown in Figure 2, and their coordinates are given in Table 1. A background observation was also made off the galaxy along the minor axis for use in background subtraction from the data cubes.

For our observations we used the IRS Short-Low (SL) and Long-Low (LL) modules, which cover wavelengths from 5 to 21 microns. The Low modules have resolving power in the range 60–130. Each low-resolution module is divided into two sub-slits which provide spectroscopy in either first or second order. They are denoted as SL1 ($7.5 - 14.5\ \mu\text{m}$), SL2 ($5.2 - 7.6\ \mu\text{m}$), LL1 ($20.5 - 38.5\ \mu\text{m}$, not used in these observations), and LL2 ($14.5 - 20.75\ \mu\text{m}$). All M31 regions were

Table 1. Spitzer/IRS Target Locations in M31

| Name | R.A. (J2000) | Decl. (J2000) | R_{gc}^b | $12 + \log(O/H)^c$ |
|-----------------------|---|---------------|------------|--------------------|
| Nucleus ^a | 00 ^h 42 ^m 44 ^s .31 | 41°16′09″.4 | 0.0 | |
| Bulge ^a | 00 ^h 42 ^m 35 ^s .00 | 41°21′01″.0 | 4.7 | 8.90 ± 0.03 |
| Region 1 | 00 ^h 41 ^m 30 ^s .41 | 40°43′07″.8 | 12.4 | 9.20 ± 0.20 |
| Region 2 | 00 ^h 45 ^m 22 ^s .85 | 41°38′53″.1 | 13.0 | 9.07 ± 0.02 |
| Region 3 | 00 ^h 40 ^m 37 ^s .37 | 41°01′29″.4 | 12.1 | 8.85 ± 0.01 |
| Region 4 | 00 ^h 41 ^m 17 ^s .86 | 41°07′09″.8 | 8.7 | 8.89 ± 0.06 |
| Region 5 | 00 ^h 43 ^m 39 ^s .57 | 41°19′03″.1 | 7.0 | 8.93 ± 0.08 |
| Region 6 | 00 ^h 43 ^m 35 ^s .72 | 41°23′15″.0 | 4.3 | 8.73 ± 0.08 |
| Region 7 | 00 ^h 40 ^m 53 ^s .98 | 40°58′58″.9 | 8.7 | 8.40 ± 0.08 |
| Region 8 | 00 ^h 42 ^m 21 ^s .60 | 41°07′17″.4 | 3.1 | 8.94 ± 0.08 |
| Region 9 ^a | 00 ^h 41 ^m 00 ^s .00 | 40°36′20″.3 | 13.5 | 8.86 ± 0.02 |
| NGC 206 | 00 ^h 40 ^m 20 ^s .20 | 40°44′54″.0 | 9.8 | |
| Background | 00 ^h 44 ^m 41 ^s .80 | 40°58′56″.0 | 29.5 | |

^aRegions with ISOCAM data.^bDe-projected galactocentric distance in kpc^cMetallicities from Sanders et al. (2012), except for Regions 5 and 8 where metallicities estimated from the radial metallicity profile.**Figure 2.** An 8 micron negative IRAC image of M31 (Barmby et al. 2006). Small white rectangles ($30'' \times 50''$) show the regions that we observed, and larger squares ($192'' \times 192''$) show the regions observed by Cesarsky et al. (1998).

observed in September 2007 as part of G. G. Fazio’s Guaranteed Time (program ID 40032). The map size was based on the size of the IRS slits (SL: $3.6'' \times 57''$, LL: $10.5'' \times 168''$). Each region was covered by 18 overlapping observations of the SL slit and 11 overlapping observations of the LL slit making the map size $32'' \times 57''$ for SL and $58'' \times 168''$ for LL. Figure 3 shows an example of the slit arrangement. For the brighter regions (nucleus, bulge), ramp times of 14 s (SL) and 30 s (LL) were used, while for the fainter regions, ramp times of 60 and 120 s were used respectively. Background observations were taken with each module (2 per ramp time). Because all of the targets are in the same part of the sky, a common background observation was used for multiple targets to subtract the background emission.

2.2 IRS Data Reduction

The data were reduced through the SSC pipeline (ver. S17.2.0), and the maps were assembled using the CUBISM program (Smith et al. 2007a). Bad pixel removal was also

done using CUBISM, and the background observations were used to subtract the background emission from these cubes following the method outlined by Gordon et al. (2008). Spectra were extracted using a $30'' \times 50''$ rectangular aperture, which corresponds to 114×190 pc at the distance of M31. The aperture size was selected to cover the overlapping area of the SL and LL modes; all the IRS maps cover more area than considered here. In order to study the spatial variation of the emission near the nucleus, we also extracted spectra from two smaller regions within that map; these will be further discussed in Section 4.4. The spectrum of NGC 206 is very noisy and was removed from our analysis.

There is wavelength overlap between the SL1 and SL2 spectra and also between the SL1 and LL2 spectra. To generate a single spectrum for each M31 region it is necessary to combine the spectra and account for photometric offsets between them. We first combined the extracted SL1 and SL2 spectra by computing the average flux densities over the wavelength overlap region ($7.5 < \lambda < 7.6 \mu\text{m}$), adding a constant to the SL2 spectra so that they matched the SL1

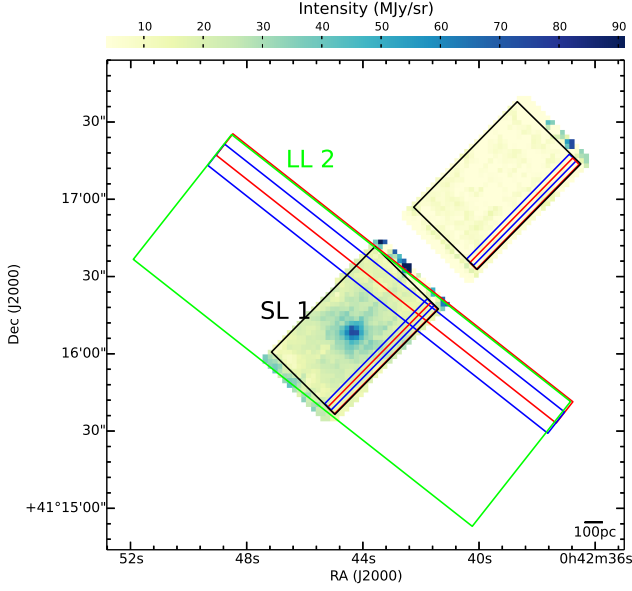


Figure 3. The $7.6\ \mu\text{m}$ plane constructed from the SL1 data cube of the nucleus, showing the arrangement of slits used to cover the region. Black boxes outline the footprint of the SL1 maps (the off-center SL1 map is from observations made when SL2 was centred) and the green box outlines the LL2 map. Blue and red slits show how each map was covered using overlapping slit positions.

average, and averaging the SL1 + shifted SL2 spectra over the overlap region. After this procedure there was still a noticeable mis-match between the SL and LL spectra. We addressed this by scaling the SL spectra to match IRAC $8\ \mu\text{m}$ fluxes as follows. IRAC fluxes were measured on the $8\ \mu\text{m}$ image (Barmby et al. 2006) in the same apertures used to extract the IRS spectra. The extended source aperture correction of 0.824 was applied to the IRAC fluxes. The standard deviation of the IRAC flux in a region similar in size but off the disk of the galaxy ($00^{\text{h}}48^{\text{m}}58^{\text{s}}.0, +42^{\circ}14'54''.0$) was used to estimate the IRAC photometric uncertainties. The *Spitzer* synthetic photometry software (Spitzer Science Center 2012) was then used to quantify the colour correction for each spectrum, i.e. the multiplicative factor K between the IRAC photometry over its broad bandpass and the IRS flux density at the centre of the bandpass. The IRAC photometry, IRS flux density, and colour corrections for each region are given in Table 2. Plotting the IRS and colour-corrected IRAC measurements (Figure 4) and fitting a straight line weighted by the uncertainties, we found that the best-fit relation between the measurements had a slope of 0.81 ± 0.08 and intercept of -0.05 ± 0.06 . The non-zero intercept of this fit suggested that an additive offset was more appropriate for combining SL and LL spectra than a multiplicative one; this method was also used by Sandstrom et al. (2012). Therefore we scaled each SL spectrum by an offset

$$x = F_{\text{IRAC}}/K - F_{\text{IRS}} \quad (1)$$

where the individual offsets are given in Table 2. The scaled SL spectra were much better matched to the LL spectra, and the final combination of SL and LL was done using the

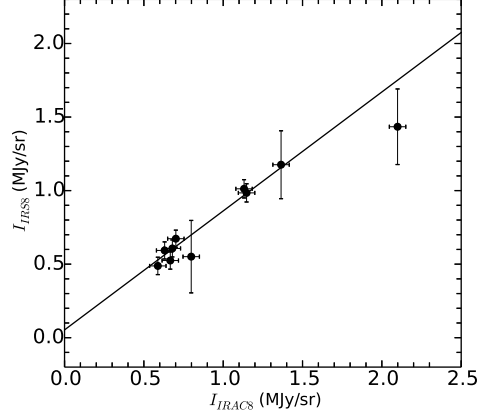


Figure 4. Intensity of the aperture corrected IRAC $8\ \mu\text{m}$ image versus that of the colour-corrected IRS spectra at $8\ \mu\text{m}$ obtained using the same aperture for our regions in M31. The straight line is the line of best fit.

Table 2. Matched aperture photometry

| Name | IRS ^a MJy sr ⁻¹ | IRAC ^b MJy sr ⁻¹ | K^c | Offset x^d MJy sr ⁻¹ |
|----------|--|---|-------|--------------------------------------|
| Region 1 | 1.8505 | 1.3923 | 0.532 | 0.3061 |
| Region 2 | 1.8238 | 1.3731 | 0.555 | 0.2148 |
| Region 3 | 0.7192 | 0.9689 | 0.767 | 0.3218 |
| Region 4 | 1.1431 | 0.8513 | 0.589 | 0.0407 |
| Region 5 | 0.6787 | 0.8088 | 0.773 | 0.1834 |
| Region 6 | 0.6399 | 0.7656 | 0.927 | 0.0479 |
| Region 7 | 1.1538 | 0.8243 | 0.526 | 0.1380 |
| Region 8 | 0.5556 | 0.7135 | 0.877 | 0.1148 |
| Region 9 | 1.9413 | 1.6562 | 0.606 | 0.3107 |
| Bulge | 2.6956 | 2.5473 | 0.532 | 1.2425 |

^aSpecific intensity measured at $8.00\ \mu\text{m}$, no colour correction.

^bSpecific intensity measured over the IRAC $8\ \mu\text{m}$ bandpass, no extended source correction.

^cColour correction factor computed from IRS spectrum.

^dComputed offset between IRAC and IRS as defined in Eq. 1.

average-and-offset procedure described above for SL1 and SL2.

2.3 ISOCAM Data Reduction

To compare our results with those of Cesarsky et al. (1998), we retrieved the highly processed ISOCAM data provided by Boulanger et al. (2005) for the nucleus, bulge, and region 9. The ISOCAM data were obtained with the circular variable filters (CVFs) over a $3' \times 3'$ field of view at a scale of $6''$ per pixel. The wavelength range covered was $5.15\text{--}16.5\ \mu\text{m}$ at a resolution of $\lambda/\Delta\lambda \approx 45$; the ISOCAM instrument is described by Cesarsky et al. (1996). An example image of the ISOCAM data is shown in Figure 5. For the three regions, we extracted spectra using the same $30'' \times 50''$ aperture as for the IRS data.

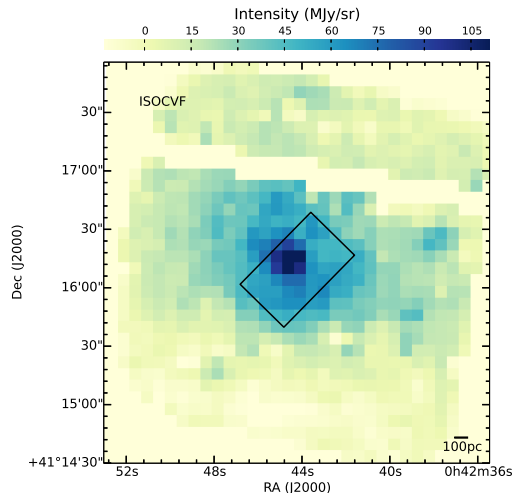


Figure 5. 11.3 μm negative image (dark colours indicate higher flux) of the ISOCAM data cube from the nucleus of M31. The black box shows the size of the aperture ($30'' \times 50''$) used to extract spectra.

3 SPECTRAL CHARACTERISTICS AND FEATURE MEASUREMENTS

The final processed IRS spectra are shown in Figure 6, except for the nucleus, discussed in Section 4.4. All of the main PAH features, including the 6.2, 7.7, 8.6 and 11.3 μm bands, are clearly visible for all the regions shown here. The IRS spectra also show atomic line emission such as [Ar II], [Ar III], [S III], [S IV], [Ne II], [Ne III] and molecular H_2 emission at 12.3 μm . Some of the spectra display a contribution to the continuum from starlight emission.

3.1 ISOCAM versus IRS

As mentioned in the Introduction, based on ISOCAM observations of four regions in M31, Cesarsky et al. (1998) reported suppression of the common 6–8 μm PAH bands and a strong 11.3 μm PAH band. The 11.3 μm band profile was found to vary from region to region. In addition, Pagani et al. (1999) confirmed that the star-forming ring in M31 shows very weak PAH emission in the 6 to 8 μm region. However, the IRS spectra presented here do not show such unusual behaviour (Figure 6). Indeed, all regions show a normal mid-infrared spectrum similar to other nearby star-forming galaxies.

Until 2005, ISOCAM-CVF data were not properly background subtracted and they were contaminated with zodiacal emission and stray light. Differential spectra between regions of relatively strong and weak emission were previously used to overcome this problem (more details about the differential spectra are given by Cesarsky et al. 1998, Pagani et al. 1999). In 2005, all ISOCAM-CVF data were reprocessed and corrected for the zodiacal emission (Boulanger et al. 2005). We obtained newly-processed ISOCAM spectra from three regions in our IRS sample (see Section 2.3) in order to compare them with the corresponding IRS spectra. Figure 7 shows that although the relative feature intensities in the IRS and ISOCAM spectra differ in detail, the spectral

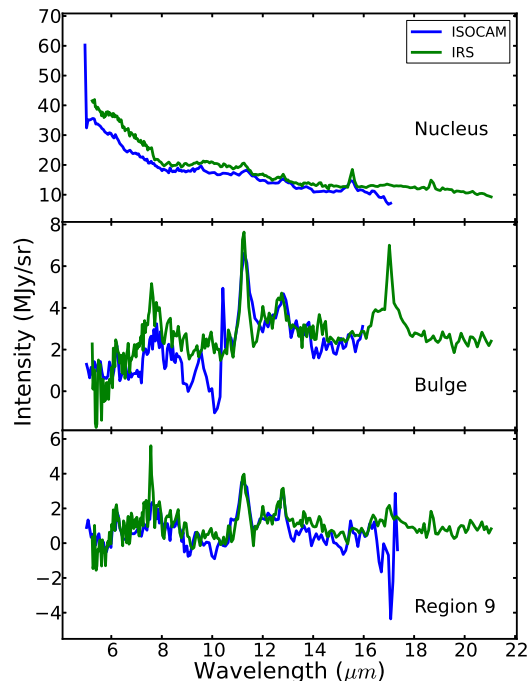


Figure 7. Comparison of IRS and re-processed ISOCAM spectra for the Nucleus (top), Bulge (middle) and Region 9 (bottom) in M31.

shapes are almost identical; the re-processed ISOCAM data do not agree with the previous differential spectra. Neither the bulge nor Region 9 shows any depletion in 6 to 8 μm features as described by Cesarsky et al. (1998). The new ISOCAM reduction appears to eliminate the discrepancies between ISOCAM and IRS, resulting in less ‘strange’ infrared spectra for M31. For the remainder of this work, we discuss only the IRS spectra.

3.2 PAHFIT

The PAH features in IRS spectra are often blended with neighbouring PAH features and atomic lines. Therefore measuring the strength of PAH features is difficult. To achieve this task a tool called PAHFIT, introduced by Smith et al. (2007b), was used. PAHFIT is an IDL based tool designed for decomposing *Spitzer* IRS low-resolution spectra of PAH emission sources. PAHFIT uses six main components to fit the surface brightness. These are starlight continuum, featureless thermal dust continuum, pure rotational lines of H_2 , fine-structure lines, dust emission features and dust extinction. The starlight is represented by blackbody emission at a fixed temperature of 5000 K, and the dust continuum is represented by 8 modified blackbodies (emissivity proportional to ν^2) at fixed temperatures of 35, 40, 50, 65, 90, 135, 200, and 300 K. The final fit obtained with PAHFIT does not necessarily use all eight dust components. The infrared extinction is considered as a combination of a power law plus silicate absorption features with peaks at 9.7 and 18 μm . Line features are represented by Gaussian profiles with widths set by the instrumental resolution and dust fea-

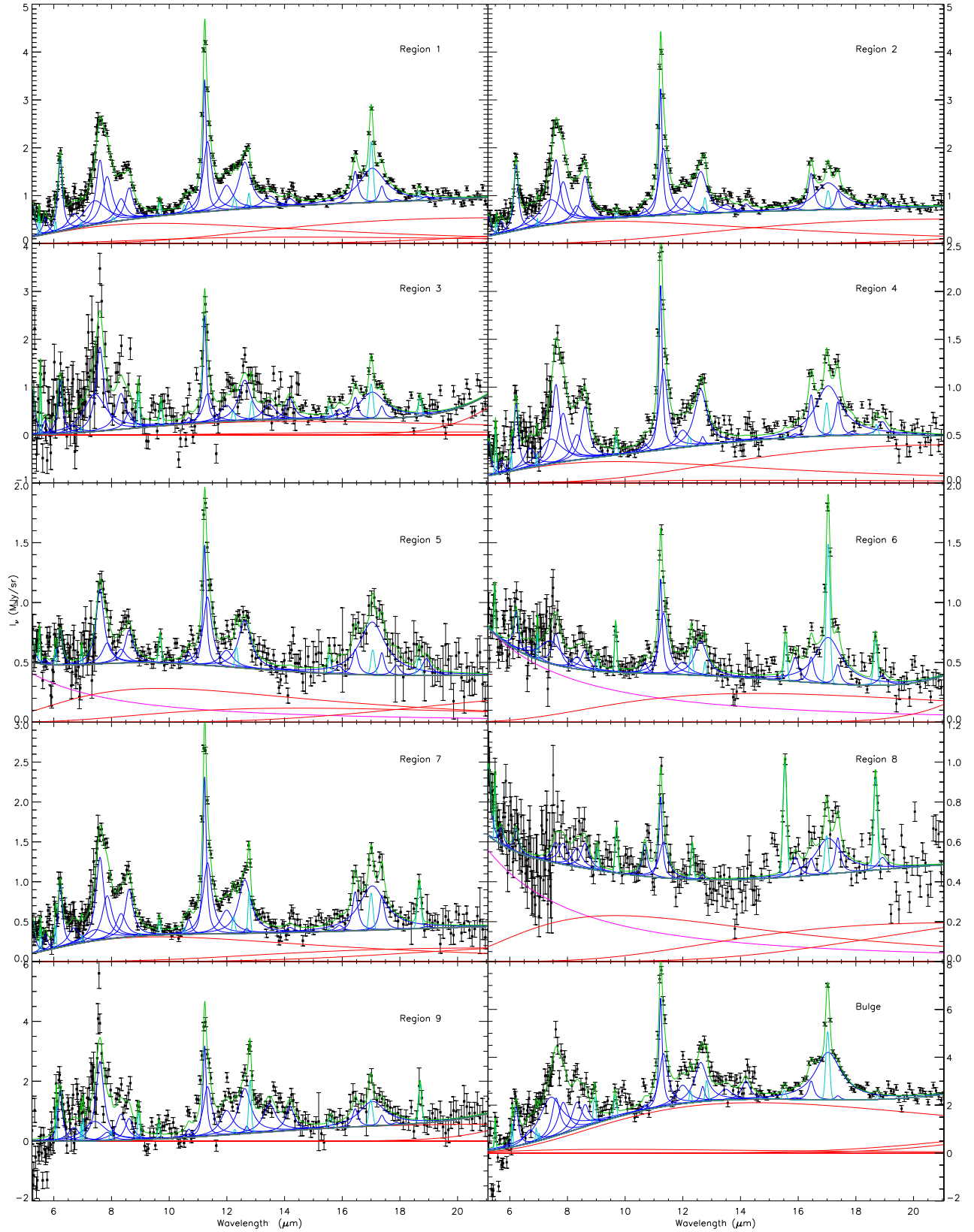


Figure 6. Observed IRS spectra and detailed PAHFIT decompositions (see Section 3.2). Regions are labeled in each panel. Black squares show the observed data, and red, blue, light blue, pink and green lines represent the modelled dust continua, PAH features, atomic lines, starlight continuum and the fit respectively. The black line shows the total modelled continuum. Vertical scales differ in different panels. Spectra from the nucleus and NGC 206 are not shown here.

tures are represented by Drude profiles; more details about PAHFIT are given by Smith et al. (2007b).

Initial attempts at fitting the spectra with PAHFIT showed that some components were negligible, and to avoid over-fitting we re-ran the fits without these components. None of the IRS spectra shows significant silicate absorption around 9.7 or 18 μm , and the extinction calculated by PAHFIT was almost zero for all the initial fits. Except for four regions (the bulge, Region 5, Region 6 and Region 8), the starlight contribution is also negligible. We adjusted the PAHFIT input parameters to fix extinction to zero for all regions and starlight to zero for all but the four regions above. Typically only two or three thermal dust components had significant power in our fits, but we did not fix the unused components to zero. Regions 3 and 9 were found to have very low dust continuum emission compared to other spectra, possibly because of noisy data at short wavelengths. However the other features in these spectra appear to be fit correctly. The spectrum of the nucleus shows silicate emission (see Section 4.4), which is not included in PAHFIT; consequently PAHFIT was unable to successfully fit the other spectral features in this spectrum.

3.3 PAH features

PAHFIT returns fluxes and equivalent widths (EQWs) of PAH features, which are given in Tables 3 and 4. For easier comparison with previous work, the tables give measurements for the 7.7, 11.3, 12.7 and 17.0 μm PAH complexes as defined by Smith et al. (2007b), as computed from the individual constituent features measured by PAHFIT. The intensities of the features do not include any contribution from the continuum, but the equivalent width computed by

$$\text{EQW} = \int \frac{I_{\nu, \text{feature}}}{I_{\nu, \text{cont}}} d\lambda, \quad (2)$$

is a measure of the ratio of the continuum emission ($I_{\nu, \text{cont}}$) to the line strength ($I_{\nu, \text{feature}} = I_{\nu} - I_{\nu, \text{cont}}$). The continuum emission is mainly from dust grains, much larger than PAH molecules. Hence, by studying EQWs of PAHs, we can study how the PAHs compete with the dust grains in the mid-infrared wavelengths. PAHFIT returns the EQWs for each PAH feature, we calculated the uncertainties using a Monte-Carlo method. In that method, for each region, PAHFIT was run 500 times on randomly generated data points normally distributed within the uncertainties of the spectrum. PAHFIT returned 500 EQWs for each PAH feature, and the standard deviation of EQWs for a given feature was taken as its uncertainty. The EQWs from Regions 3 and 9 were removed from further analysis because the negligible dust continuum for these spectra makes the EQWs highly uncertain.

3.4 Atomic line features

PAHFIT also returns the line strengths and uncertainties for atomic lines, listed in Table 5. Not all lines were detected by PAHFIT, so we calculated upper limits for non-detected

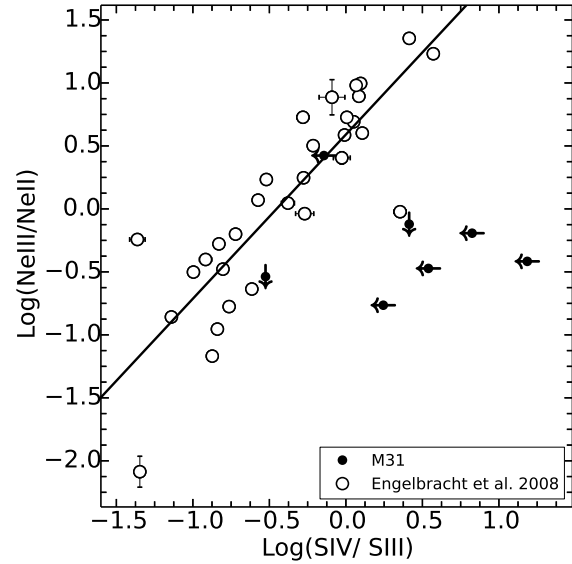


Figure 8. $\text{Log}([\text{Ne III}]/[\text{Ne II}])$ vs $\text{log}([\text{S IV}]/[\text{S III}])$ for the M31 regions in our sample (black dots) and the starburst sample from Engelbracht et al. (2008) (open dots). The straight line is the line of best fit for the starburst sample. Upper limits are 3σ .

lines.¹ Line ratios of $[\text{Ne III}]/[\text{Ne II}]$ and $[\text{S IV}]/[\text{S III}]$ 18 have been used as an indication of the radiation hardness, and Engelbracht et al. (2008) defined a combination of these two line ratios as a ‘radiation hardness index (RHI)’:

$$\text{RHI} = \left(\log \frac{[\text{Ne III}]}{[\text{Ne II}]} + \left[0.71 + 1.58 \log \frac{[\text{S IV}]}{[\text{S III}]} \right] \right) / 2 \quad (3)$$

Here, 1.58 and 0.71 are the slope and intercept of the $[\text{Ne III}]/[\text{Ne II}]$ vs $[\text{S IV}]/[\text{S III}]$ plot (Figure 8) for the starburst sample from Engelbracht et al. (2008). The RHI has also been used by Gordon et al. (2008) for M101 observations. Figure 8 compares the atomic line emission from the selected regions of M31 to the starburst galaxy sample; although none of our spectra have detections of all four lines, our limits are mostly consistent with the trend. We therefore compute the RHI using the first term of equation 3.4 for the regions with missing S lines and the second term for the regions with missing Ne lines. Regions 2, 5, and 8 had detections of only one line per element, so we used the appropriate upper limits to calculate RHI for these spectra.

4 RESULTS AND DISCUSSION

4.1 PAH intensities

Both the 6.2 and 7.7 μm features are thought to be coming from ionized PAHs and the 11.3 μm feature from neutral PAHs. Therefore we expect to see a correlation between the

¹ To find the upper limits for the flux of missing atomic lines, we assumed the line to be a Gaussian profile with a FWHM as given by PAHFIT. The peak intensity was taken to be 3 times the RMS, where RMS is the root mean square of the noise at the position of a missing line.

Table 3. PAH Emission Line Strengths^a

| Region | 5.7 μm | 6.2 μm | 7.7 μm^b | 8.3 μm | 8.6 μm | 10.7 μm | 11.3 μm^b | 12.0 μm | 12.7 μm^b | 17.0 μm^b |
|----------|-------------------|-------------------|---------------------|-------------------|-------------------|--------------------|----------------------|--------------------|----------------------|----------------------|
| Bulge | ... | 1.32 \pm 0.08 | 7.7 \pm 0.6 | 1.1 \pm 0.2 | 0.7 \pm 0.1 | 0.07 \pm 0.03 | 1.85 \pm 0.08 | 0.49 \pm 0.05 | 1.02 \pm 0.09 | 1.39 \pm 0.04 |
| Region 1 | 0.36 \pm 0.05 | 1.20 \pm 0.04 | 3.8 \pm 0.2 | 0.46 \pm 0.04 | 0.50 \pm 0.03 | 0.08 \pm 0.01 | 1.18 \pm 0.02 | 0.32 \pm 0.02 | 0.54 \pm 0.02 | 0.58 \pm 0.02 |
| Region 2 | 0.27 \pm 0.03 | 1.10 \pm 0.03 | 3.7 \pm 0.2 | 0.33 \pm 0.04 | 0.70 \pm 0.03 | 0.053 \pm 0.008 | 1.13 \pm 0.02 | 0.23 \pm 0.01 | 0.51 \pm 0.03 | 0.51 \pm 0.02 |
| Region 3 | 0.3 \pm 0.1 | 0.9 \pm 0.1 | 3.9 \pm 0.6 | 0.7 \pm 0.1 | 0.3 \pm 0.1 | ... | 0.68 \pm 0.07 | 0.21 \pm 0.05 | 0.47 \pm 0.07 | 0.45 \pm 0.04 |
| Region 4 | 0.14 \pm 0.04 | 0.56 \pm 0.03 | 2.1 \pm 0.2 | 0.26 \pm 0.04 | 0.41 \pm 0.03 | 0.029 \pm 0.008 | 0.70 \pm 0.02 | 0.12 \pm 0.01 | 0.31 \pm 0.02 | 0.44 \pm 0.02 |
| Region 5 | ... | 0.24 \pm 0.04 | 0.79 \pm 0.07 | 0.12 \pm 0.04 | 0.21 \pm 0.03 | 0.032 \pm 0.008 | 0.45 \pm 0.02 | 0.09 \pm 0.01 | 0.22 \pm 0.01 | 0.33 \pm 0.04 |
| Region 6 | ... | 0.26 \pm 0.03 | 0.8 \pm 0.2 | 0.10 \pm 0.03 | 0.13 \pm 0.03 | 0.029 \pm 0.008 | 0.38 \pm 0.02 | 0.07 \pm 0.01 | 0.16 \pm 0.01 | 0.29 \pm 0.02 |
| Region 7 | 0.21 \pm 0.03 | 0.62 \pm 0.03 | 2.0 \pm 0.2 | 0.30 \pm 0.04 | 0.45 \pm 0.03 | 0.058 \pm 0.008 | 0.77 \pm 0.02 | 0.18 \pm 0.01 | 0.37 \pm 0.03 | 0.47 \pm 0.04 |
| Region 8 | ... | 0.09 \pm 0.04 | 0.22 \pm 0.07 | 0.09 \pm 0.04 | 0.10 \pm 0.03 | 0.051 \pm 0.009 | 0.16 \pm 0.02 | ... | ... | 0.15 \pm 0.02 |
| Region 9 | ... | 1.3 \pm 0.1 | 4.4 \pm 0.6 | 0.9 \pm 0.1 | 0.5 \pm 0.1 | 0.09 \pm 0.03 | 1.32 \pm 0.07 | 0.51 \pm 0.05 | 0.83 \pm 0.07 | 0.6 \pm 0.1 |

^aUnits are $10^{-15} \text{ W m}^{-2}$.^bPAH complexes, as described in text.**Table 4.** PAH Emission Line Equivalent Widths^a

| Region | 5.7 μm | 6.2 μm | 7.7 μm^b | 8.3 μm | 8.6 μm | 10.7 μm | 11.3 μm^b | 12.0 μm | 12.7 μm^b | 17.0 μm^b |
|----------|-------------------|-----------------------------|-----------------------------|-------------------|-------------------|--------------------|----------------------|--------------------|----------------------|----------------------|
| Bulge | ... | 1.2 \pm 0.2 | 4.1 \pm 0.4 | 0.51 \pm 0.07 | 0.30 \pm 0.06 | 0.03 \pm 0.01 | 0.78 \pm 0.04 | 0.22 \pm 0.02 | 0.49 \pm 0.05 | 1.16 \pm 0.04 |
| Region 1 | 0.39 \pm 0.08 | 1.2 \pm 0.1 | 3.4 \pm 0.3 | 0.43 \pm 0.04 | 0.47 \pm 0.04 | 0.09 \pm 0.01 | 1.45 \pm 0.04 | 0.43 \pm 0.03 | 0.76 \pm 0.04 | 1.26 \pm 0.05 |
| Region 2 | 0.28 \pm 0.04 | 1.02 \pm 0.06 | 3.4 \pm 0.2 | 0.32 \pm 0.04 | 0.70 \pm 0.04 | 0.07 \pm 0.01 | 1.58 \pm 0.04 | 0.35 \pm 0.02 | 0.85 \pm 0.05 | 1.33 \pm 0.06 |
| Region 3 | 4.3 \pm 2.3 | 8.3 \pm 2.3 | 18.5 \pm 4.2 | 2.8 \pm 0.8 | 0.9 \pm 0.5 | ... | 2.1 \pm 0.3 | 0.7 \pm 0.2 | 1.6 \pm 0.3 | 2.4 \pm 0.3 |
| Region 4 | 0.28 \pm 0.09 | 1.0 \pm 0.1 | 3.7 \pm 0.4 | 0.48 \pm 0.07 | 0.77 \pm 0.07 | 0.07 \pm 0.02 | 1.67 \pm 0.06 | 0.31 \pm 0.04 | 0.82 \pm 0.06 | 1.65 \pm 0.08 |
| Region 5 | ... | 0.12 \pm 0.03 | 0.61 \pm 0.07 | 0.10 \pm 0.03 | 0.20 \pm 0.03 | 0.05 \pm 0.01 | 0.77 \pm 0.04 | 0.17 \pm 0.03 | 0.50 \pm 0.04 | 1.6 \pm 0.2 |
| Region 6 | ... | 0.10 \pm 0.04 | 0.6 \pm 0.2 | 0.10 \pm 0.04 | 0.14 \pm 0.03 | 0.05 \pm 0.01 | 0.77 \pm 0.05 | 0.15 \pm 0.03 | 0.42 \pm 0.05 | 1.7 \pm 0.1 |
| Region 7 | 0.32 \pm 0.05 | 0.86 \pm 0.06 | 2.2 \pm 0.1 | 0.44 \pm 0.06 | 0.69 \pm 0.06 | 0.12 \pm 0.02 | 1.81 \pm 0.07 | 0.48 \pm 0.05 | 1.08 \pm 0.09 | 2.2 \pm 0.3 |
| Region 8 | ... | ... | 0.10 \pm 0.05 | 0.09 \pm 0.04 | 0.10 \pm 0.03 | 0.09 \pm 0.02 | 0.30 \pm 0.04 | ... | ... | 0.62 \pm 0.08 |
| Region 9 | ... | $(2.4 \pm 1.1) \times 10^2$ | $(1.4 \pm 0.4) \times 10^2$ | 15.5 \pm 5.6 | 7.9 \pm 2.8 | 0.5 \pm 0.2 | 6.8 \pm 1.1 | 2.3 \pm 0.6 | 3.5 \pm 0.8 | 2.2 \pm 0.8 |

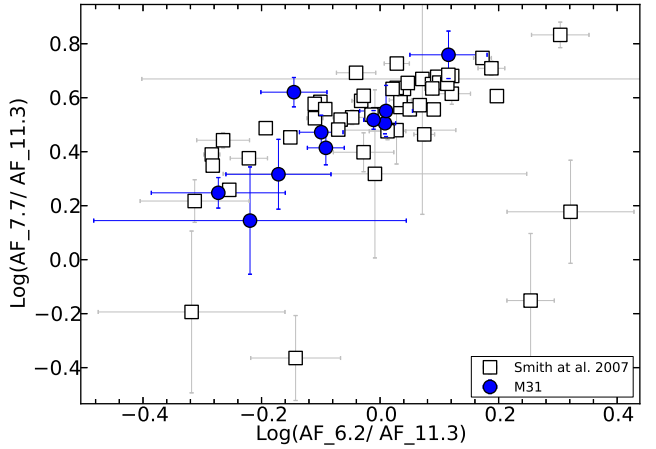
^aUnits are μm .^bPAH complexes, as described in text.

Continuum for Regions 3 and 9 is very weak. Equivalent widths are highly uncertain and not considered in the analysis (see Section 3).

intensities of 6.2 and 7.7 μm PAH features normalized by the 11.3 μm feature. Figure 9 compares the PAH flux ratios of 7.7/11.3 and 6.2/11.3 features. The figure shows a good correlation between these two PAH line ratios, consistent with that of the SINGS sample shown by Smith et al. (2007b). A similar correlation was also reported by Galliano et al. (2008b) for a sample of galaxies and a handful of extended H II regions and by Vermeij et al. (2002) for Galactic and Magellanic Cloud I regions. This provides evidence that the PAH emission from M31 is not unusual.

4.2 PAH equivalent widths versus radiation hardness

As mentioned in the introduction, PAH equivalent widths tend to show an inverse correlation with radiation hardness. The equivalent widths of the M31 PAH features are compared with RHI in Figures 10 and 11. For reference, we also show the starburst sample of Engelbracht et al. (2008) and the seven H II regions in M101 observed by Gordon et al. (2008). To make a direct comparison with the M101 sample, we normalized the M31 EQWs in Figure 11 using the same procedure as Gordon et al. (2008), dividing each EQW by the weighted average over all regions in the respective samples. The equivalent widths seem to be decreasing with increasing radiation hardness, consistent with previous results. This also helps to confirm that the PAH emission in M31 is not unusual.

**Figure 9.** Ratios of PAH feature fluxes (7.7 $\mu\text{m}/11.3 \mu\text{m}$ versus 6.2 $\mu\text{m}/11.3 \mu\text{m}$) for 10 regions in M31. Open squares represent the central regions of nearby galaxies as observed in the SINGS sample by Smith et al. (2007b).

4.3 PAH equivalent widths versus metallicity

Many studies based on ISO and *Spitzer* observations have reported that PAH intensity decreases with decreasing metallicity (Calzetti et al. 2010). In addition, these studies also report a sudden drop of EQWs of PAHs around $12 + \log(\text{O}/\text{H}) \approx 8.1$. This has been observed amongst different galaxies (Engelbracht et al. 2008) as well as within a single galaxy (Gordon et al. 2008).

Table 5. Atomic Emission Line Strengths^a

| Region | [Ar II] 7.0 μm | [Ar III] 9.0 μm | [S IV] 10.5 μm | [Ne II] 12.8 μm | [Ne III] 15.5 μm | [S III] 18.7 μm |
|----------|------------------------------|-------------------------------|------------------------------|-------------------------------|--------------------------------|-------------------------------|
| Bulge | < 0.12 | 0.17 ± 0.03 | < 0.11 | 0.07 ± 0.01 | 0.025 ± 0.006 | 0.007 ± 0.003 |
| Region 1 | < 0.05 | < 0.06 | 0.020 ± 0.004 | 0.020 ± 0.004 | < 0.01 | 0.008 ± 0.001 |
| Region 2 | < 0.05 | < 0.06 | < 0.02 | 0.022 ± 0.004 | < 0.01 | 0.003 ± 0.002 |
| Region 3 | < 0.15 | 0.09 ± 0.02 | < 0.10 | 0.03 ± 0.01 | 0.020 ± 0.004 | 0.015 ± 0.003 |
| Region 4 | < 0.04 | < 0.04 | < 0.02 | < 0.02 | < 0.01 | 0.004 ± 0.002 |
| Region 5 | < 0.04 | < 0.02 | < 0.02 | < 0.01 | 0.009 ± 0.004 | 0.008 ± 0.004 |
| Region 6 | 0.02 ± 0.01 | 0.014 ± 0.007 | < 0.01 | < 0.01 | 0.019 ± 0.002 | 0.019 ± 0.002 |
| Region 7 | < 0.04 | < 0.04 | 0.008 ± 0.003 | 0.035 ± 0.005 | < 0.01 | 0.027 ± 0.004 |
| Region 8 | < 0.04 | 0.017 ± 0.006 | < 0.02 | < 0.01 | 0.041 ± 0.002 | 0.023 ± 0.002 |
| Region 9 | 0.09 ± 0.04 | 0.12 ± 0.03 | < 0.09 | 0.13 ± 0.01 | < 0.04 | 0.05 ± 0.02 |

^aUnits are $10^{-15} \text{ W m}^{-2}$. Upper limits (3σ) are indicated with a < mark.

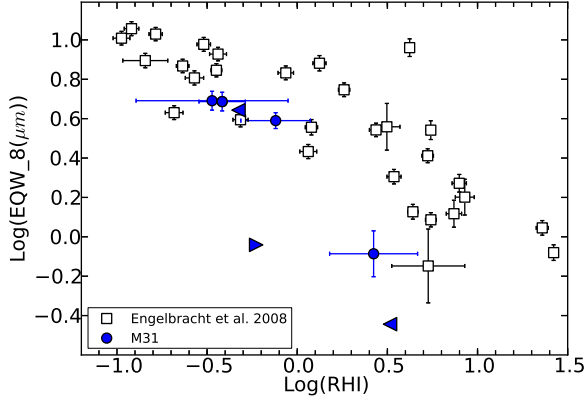


Figure 10. Equivalent width of the 8 μm PAH feature versus radiation hardness index (RHI) for the M31 sample (blue). The 8 μm feature is a combination of the 7.7, 8.3 and 8.6 μm PAHFIT components. Open squares represent the starburst galaxy sample from Engelbracht et al. (2008), which includes 66 nearby ($2 < d < 250$ Mpc) star-bursting or star-forming galaxies selected to cover a wide range in metallicity ($7.1 < 12 + \log [\text{O}/\text{H}] < 8.9$). For M31 spectra with undetected lines, triangles represent 3σ upper (left-pointing triangles) and lower (right-pointing triangles) limits.

Sanders et al. (2012) measured spectroscopic metallicities for more than 250 H II regions using strong line diagnostics.² Except for regions 5 and 8, all of our mapped regions contain an H II region measured by Sanders et al. (2012), and we give the corresponding metallicities in Table 1. For regions 5 and 8 we adopted metallicities from the radial metallicity profile of M31 given by Sanders et al. (2012). It is well known that there are systematic differences between different methods used to measure metallicities, and those in the sample of Engelbracht et al. (2008) were obtained by the direct electron temperature method (Skillman et al. 1998). Croley et al. (2014) calculated the offset between

² Sanders et al. (2012) considered several different calibrations for abundance diagnostics. We use the results from the method they denote “N06 N2” (Nagao et al. 2006) because that method has the largest sample size.

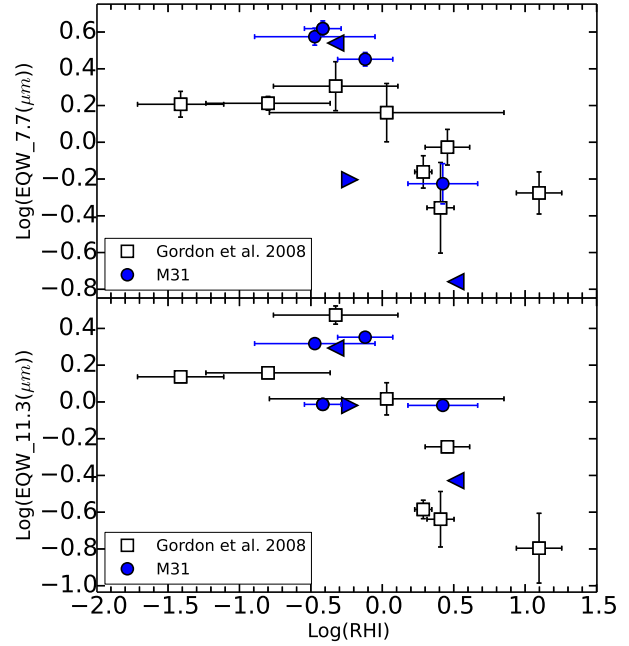


Figure 11. Equivalent widths of the normalized 7.7 μm PAH feature (top panel) and 11.3 μm PAH feature (bottom panel) versus radiation hardness index (RHI) for the M31 sample. Open squares represent the seven H II regions in M101 observed by Gordon et al. (2008), which have $8.1 < 12 + \log [\text{O}/\text{H}] < 8.8$. The normalization was done by dividing each EQW by the weighted average over all regions in the respective samples. Triangles represent 3σ upper and lower limits.

rect and strong-line measurements for M31 H II regions to be 0.35 ± 0.10 and we correct for this in Figure 12.

Figure 12 shows the normalized EQWs of the PAH features versus the metallicity for our sample and the starburst galaxies of Engelbracht et al. (2008). The scatter in our sample is large, but the equivalent widths of the 7.7 and 11.3 μm features are consistent with those of Engelbracht et al. (2008). No trend with metallicity is seen. However, we do not have enough data from low-metallicity regions in M31 to observe the expected decrease of EQWs of PAH with the decreasing metallicity. There do seem to be some outliers which can plausibly be due to the uncertainties and the

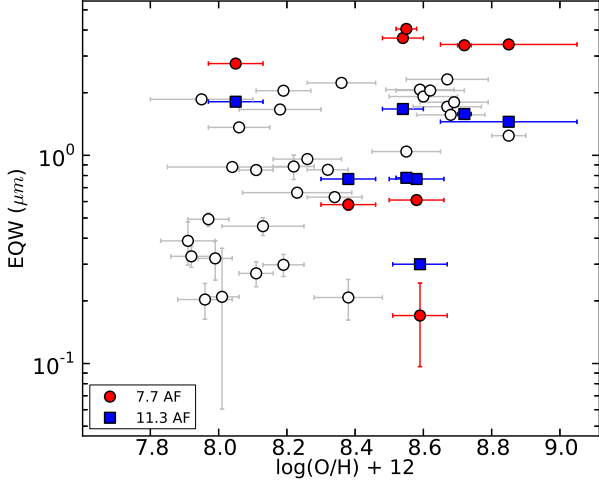


Figure 12. PAH equivalent widths versus metallicity. Filled circles are M31 7.7 μm EQWs; filled squares are M31 11.3 μm EQWs; open circles are 7.7 μm EQWs for the starburst sample from Engelbracht et al. (2008). Metallicities of the M31 regions have had 0.35 dex subtracted to account for the offset between direct and strong-line measurements.

offset between different methods of calculating the metallicity. The M31 region with very low 7.7 μm equivalent widths is Region 8, which has a noisy spectrum in the blue as well as substantial modelled contribution from starlight (see Figure 6).

4.4 Mid-infrared properties of the M31 nucleus

Examining the *Spitzer*-IRS spectral data cube for the nuclear region, we noticed that different spectral features vary spatially in the near-nuclear region. The 11.2 μm PAH emission is discrete and patchy (Figure 13 (top)). Indeed, the majority of the 11.2 μm PAH emission is from a region 15'' north of the nucleus (corresponding to *R.A., Dec.*(J2000) of (00:42:43.947, +41:16:22.92)) and not from the nucleus itself. Weaker 11.2 μm PAH emission is also found near the edge of the map peaking at (0:42:45.497, +41:15:43.97) and near (0:42:45.869; +41:16:11.38). On the other hand, the centre shows no PAH emission, but it does have silicate emission around 9.7 μm , which comes only from the nucleus and is not present in the North region (see Figure 13, middle panel).³ Finally, while [NeIII] 15.5 μm line emission is present across the nuclear region, its spatial morphology is distinct from that of the silicate and PAH emission (see Figure 13, bottom panel); although the three locations with 11.2 μm PAH emission also show enhanced [NeIII] 15.5 μm line emission. The locations of the two weaker 11.2 μm PAH emission peaks is also near positions exhibiting CO(2-1) line emission (#36 and 28, Melchior & Combes 2013, the strongest 11.2 μm PAH emission peak is outside the CO FOV). Radial profiles of both the nuclear and north sources have full widths at half maximum (FWHM) of 5–7'' depending on the wavelength

(corresponding to 19–27pc), while the SL PSF FWHM is 2.5–3''; therefore both sources are marginally spatially resolved. We extracted spectra from the centre and the North regions using 9'' \times 9'' square apertures as shown in Figure 13.

Figures 14 and 15 show the spectra extracted from the two regions near the nucleus. Both spectra show a blue continuum and atomic fine-structure lines but they exhibit distinct dust emission consistent with the spatial maps (Figure 13): PAH emission is detected in the north spectrum while silicate emission is seen towards the nucleus.

Figure 14 (top) shows the results of PAHFIT applied to the spectrum of the north region. Atomic fine-structure lines of Ne and S are detected as well as H₂ emission at 17 μm . In addition, PAH emission is clearly detected at 11.3 μm and between 15–20 μm while it is weak or absent at 6–8 μm . We compared the PAH emission with that of the HII-type galaxy NGC0337 in Figure 14 (bottom). Despite the enhanced noise level at the shorter wavelengths, it is clear that the emission shortwards of 10 μm is atypical for PAHs but rather seem to exhibit a broad plateau from \sim 6 to \sim 7.5 μm . Indeed, 6.2 μm PAH emission may be hidden in this broad plateau but the typical 7.7 and 8.6 μm are absent resulting in a decrease of the 7.7/11.2 ratio by roughly a factor of 10 compared to that of NGC0337. **CHECK THE PAH emission of the two other locations ... are they atypical ??**

The central spectrum exhibit silicate emission, blue continuum emission and fine-structure line emission of [NeII] at 12.8 μm , [NeIII] at 15.5 μm and [SIII] at 18.7 μm (Figure 15, top). We adopted PAHFIT so that it includes Gaussian profiles to represent the silicate emission and used this modified PAHFIT to fit the continuum emission of both star light and dust towards the nucleus (Figure 15, top). While the silicate emission is not well fitted due to its asymmetry, the underlying continuum is well represented by the PAHFIT results. To characterize the silicate emission profile, we compared the continuum-subtracted silicate profile with the silicate absorption profile of the Galactic centre (?) as well as the silicate emission profile observed towards the type 1 (i.e., face-on) LINER nucleus of M81 (Smith et al. 2010, Figure 15, bottom). For the latter, we adopted a spline continuum anchored at 8.36, 8.83, 24.7, 26.45, and 27.79 μm (Figure 15, middle). Compared to the silicate absorption profile towards the Galactic centre, the M31 silicate emission is clearly displaced towards longer wavelengths and the red wing is slightly less steep resulting in a slightly broader profile. This is consistent with previous results reporting that the silicate emission towards the M81 nucleus as well as towards several galaxies is redshifted and broader than the silicate absorption seen towards galactic sources (e.g. Sturm et al. 2005, 2006; Netzer et al. 2007; Smith et al. 2010). Contrasting the spectral properties of the nuclei of M31 and M81, we find that the "9.7" μm silicate emission is distinct from each other in peak position (9.9 and 10.56 μm respectively) and FWHM (2.58 and 2.79 μm respectively)⁴. Moreover, the physical size of the silicate emitting region is much smaller in M31 (19–27pc with respect to 230pc for M81).

³ The spatial resolution and pixel scale of the ISOCAM data are not sufficient to resolve these two regions.

⁴ The reported FWHM is smaller than that reported by Smith et al. (2010) as we consider the continuum-subtracted silicate emission profile

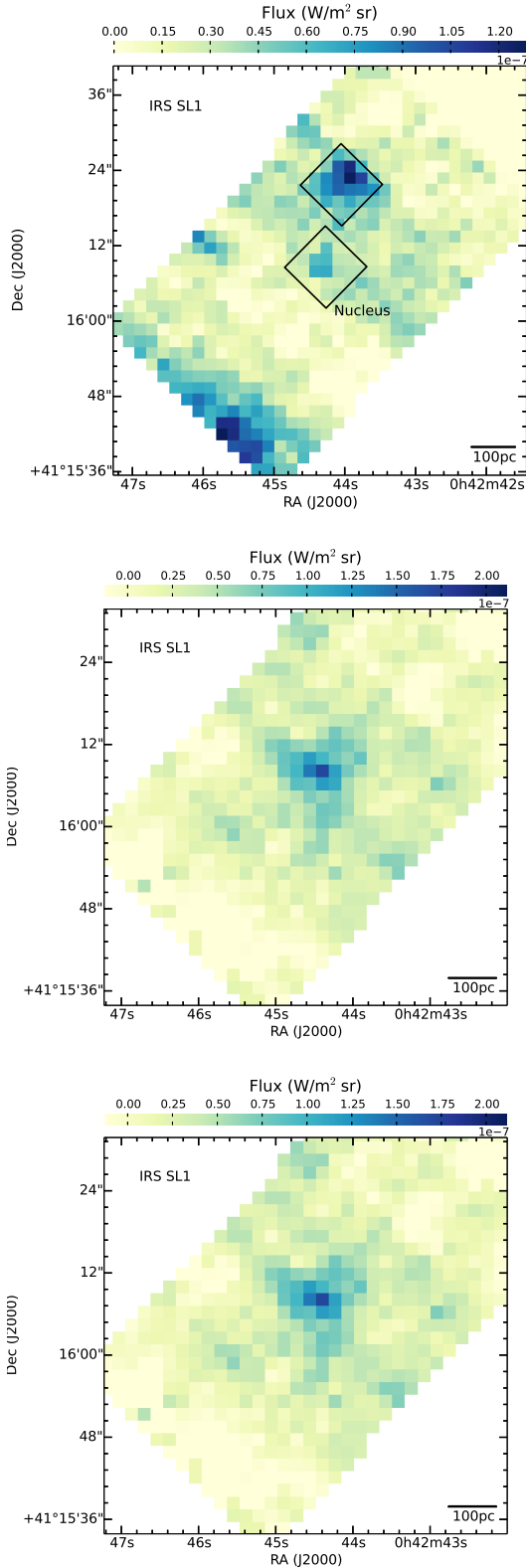


Figure 13. Integrated strength of the $11.2 \mu\text{m}$ PAH emission (top panel), the silicate emission (from 9 to $11 \mu\text{m}$, continuum subtracted; middle panel) and the $[\text{NeIII}]$ $15.5 \mu\text{m}$ line emission (bottom panel) around the nucleus of M31. As a reference, the $[\text{NeIII}]$ $15.5 \mu\text{m}$ line emission is shown as contours in each panel. The centre of the nucleus is at R.A. $00^{\text{h}}42^{\text{m}}44^{\text{s}}.35$, Dec. $+41^{\circ}16'08''.5$ (Garcia et al. 2010) and is represented by a + sign. Two black boxes are the apertures (centre and north region) used



Figure 14. Top: PAHFIT result for the extracted spectrum from the north region of the M31 nucleus: fit (orange), continuum (magenta), individual dust components (blue), individual fine-structure lines and H_2 lines (green). Bottom: Continuum subtracted spectrum of the north region compared with that of the HII-type galaxy NGC0337 (Smith et al. 2007b), normalized to the peak intensity of the $11.2 \mu\text{m}$ PAH emission. PAH emission is clearly present longward of $10 \mu\text{m}$.

And while M31 has no PAH emission in its nuclear centre, PAH emission is present across the nuclear region in M81. However, it is atypical in the same way as the PAH emission seen $15''$ North of M31's nuclear centre. Finally, also the atomic lines (e.g. $[\text{Ne II}]$ $12.8 \mu\text{m}$) are distinct between both nuclei.

Centre: "We report the detection and successful modeling of the unusual $9.7 \mu\text{m}$ SiO stretching silicate emission feature in the type 1 (i.e., face-on) LINER nucleus of M81. Using the Infrared Spectrograph (IRS) instrument on Spitzer, we determine the feature in the central 230 pc of M81 to be in strong emission, with a peak at $\sim 10.5 \mu\text{m}$. This feature is strikingly different in character from the absorption feature of the galactic interstellar medium, and from the silicate absorption or weak emission features typical of galaxies with active star formation. We successfully model the high signal-to-noise ratio IRS spectra with porous silicate dust using laboratory-acquired mineral spectra"

Figure 16 compares the full $30'' \times 50''$ M31 nuclear spectrum with the spectra extracted from the smaller regions in the centre and the North (inset, top and bottom). Also shown are nuclear spectra from six SINGS galaxies with similar spectral shapes (Smith et al. 2007b).⁵ Some SINGS galaxies share similar PAH feature characteristics to the M31 spectrum and none of them contains obvious silicate emission. Although Mason et al. (2012) reported silicate emission towards NGC4594. All of these comparison

⁵ The IRS spectra for the SINGS galaxies were extracted over areas ranging from 2 to 8 kpc^2 , whereas the M31 nucleus spectrum covers a much smaller area (0.02 kpc^2).

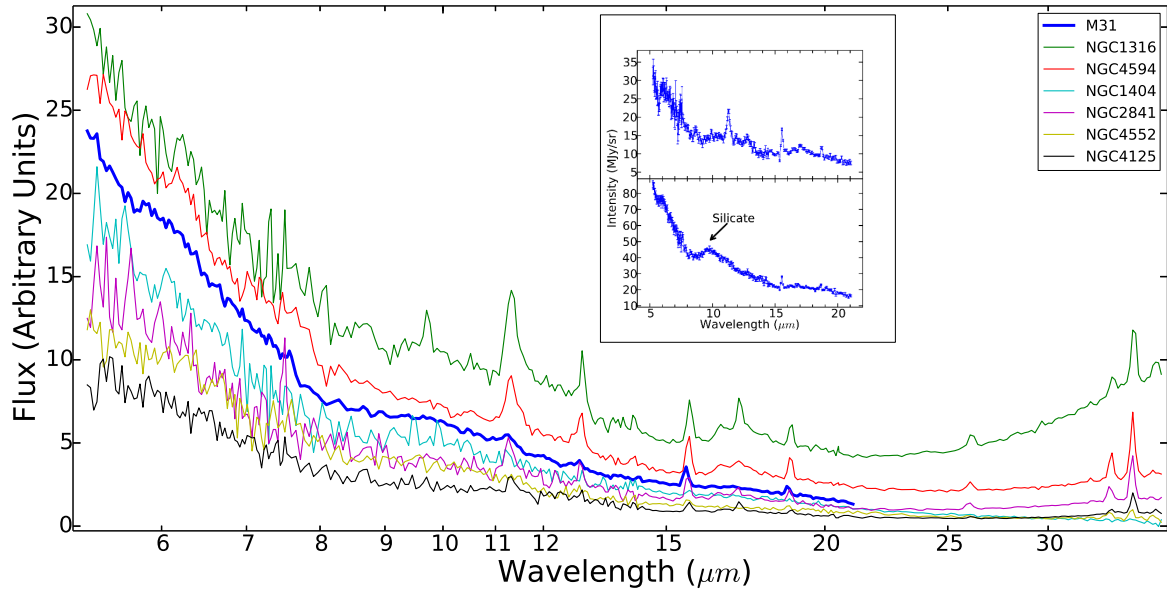


Figure 16. Mid-infrared spectrum of the nucleus of M31 (blue) over-plotted with spectra extracted close to the nuclei of 6 nearby galaxies which have AGN activity (Smith et al. 2007b). NGC 4552, NGC 1404 and NGC 4125 are elliptical galaxies and NGC 4594 and NGC 2841 are spiral galaxies. NGC 1316 is a lenticular galaxy. The inset shows the spectra extracted from the centre region of the M31 nucleus (bottom) and from the north region (top) shown in Figure 13.

galaxies have some type of low-luminosity active galactic nucleus (LLAGN). The SINGS galaxies with similar spectral shapes include three elliptical galaxies, two spirals, and a lenticular; there is some disagreement over the exact nuclear spectral types of these six galaxies (Kennicutt et al. 2003; Smith et al. 2007b; Moustakas et al. 2010). All are classified as some form of LLAGN such as Seyfert or LINER (luminous AGNs were intentionally omitted from the SINGS sample; Kennicutt et al. 2003), although they are by no means the only LLAGNs in the SINGS sample. Published estimates of the black hole masses for these galaxies range from $1.5 - 5.5 \times 10^8 M_{\odot}$ (Nowak et al. 2008; Kormendy 1988, for NGC 1316 and NGC 4595, respectively), or about $1 - 4 \times$ that of M31. M81 is classified as a LINER, with a black hole mass of $7 \times 10^7 M_{\odot}$ (Devereux et al. 2003). Li et al. (2009) concluded that the central black hole in M31 (M31*) is currently inactive, with direct observational signatures seen only at radio and X-ray wavelengths, so finding additional signatures in the mid-infrared is of great interest. To our knowledge, no such signatures have been reported; broadband mid-infrared imaging of the central regions of M31 (Davidge et al. 2006; Barmby et al. 2006) did not identify unambiguous nuclear emission. The bluest part of the spectrum in Figure ?? is dominated by the continuum, in agreement with the expectation that stellar light dominates the nucleus at these wavelengths.

Could radiation from M31* be responsible for the suppression of the 6–8 μm PAH features compared to the 11.3 μm feature? As discussed by Smith et al. (2007b) and Smith et al. (2010), inferring such a suppression must be done with caution, because the 6–8 μm features are more susceptible to dilution by the stellar continuum. Several connections between PAH suppression and the presence of an AGN are possible, including destruction of small PAH molecules by a hard radiation field, modification of the struc-

ture of the PAH molecules, or weak ultraviolet continuum from low star formation rates leading to decreased PAH excitation (Smith et al. 2007b; Diamond-Stanic & Rieke 2010). In the latter case, the AGN is not the cause of the suppressed 6–8 μm features but rather is only detectable when the nuclear star formation rate is low. Previous work has found low rates of star formation in the centre of M31: although Melchior & Combes (2013) found a significant amount of cold gas in the centre of the galaxy, this gas does not appear to be associated with current star formation (see also Li et al. 2009). In modelling the far-infrared spectral energy distribution, Groves et al. (2012) found that the old stellar population in the M31 bulge is sufficient to heat the observed dust; no young stellar population is needed. We conclude that PAH feature ratios cannot provide direct evidence for radiation from M31*.

Detection of silicate emission in the M31 nuclear spectrum is another possible indicator of nuclear accretion. Silicate emission is not very common in integrated spectra of galaxies (Spoon et al. 2007) but is seen in luminous quasar spectra (e.g. Hill et al. 2014) and, as mentioned above, in the spectrum of the M81 nucleus. In the unified model of AGNs, an obscuring torus viewed face-on would be expected to show silicate emission (Efstathiou & Rowan-Robinson 1995; Spinoglio & Malkan 1992); however such a view would also be expected to show forbidden atomic lines such as [Ne v] and [S iv], not seen in the M31 spectrum. Alternatively, Mason et al. (2012) explained that low-luminosity AGNs cannot host a Seyfert-like obscuring torus because of their optically thin dust and low dust-to-gas ratio, but can show silicate emission that originates in the optically thin hot dust around the torus. The first detection of such silicate emission was reported by Sturm et al. (2005) from the low-ionization nuclear emission-line region (LINER) galaxy NGC 3998, and Mason et al. (2012) ob-

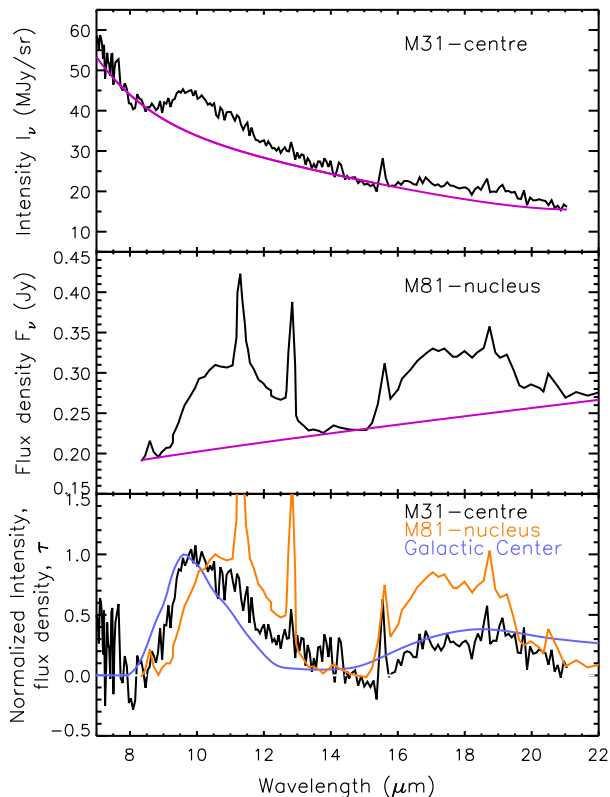


Figure 15. Top: Mid-infrared spectrum from the centre region of the M31 nucleus (black) with continuum (magenta). Middle: Mid-infrared spectrum of the nucleus of M81 ($13'' \times 13''$ aperture Smith et al. 2010, black) with continuum (magenta). Bottom: Normalized continuum-subtracted spectra of the M31 and M81 nuclei. For reference, the silicate optical depth profile towards the galactic centre is shown in blue (?).

served that $9.7 \mu\text{m}$ silicate emission is present in many LLAGNs. To quantify the magnitude of the silicate emission in mid-infrared spectra, Smith et al. (2010) defined the linear slope parameter $\gamma_{810} = [F_{\nu}(10\mu\text{m}) - F_{\nu}(8\mu\text{m})]/2F_{\nu}(9\mu\text{m})$, with positive values signifying silicate emission and negative values absorption. They found the M81 nucleus to have $\gamma_{810} = 0.37 \pm 0.04$. For the M31 centre ($9'' \times 9''$) spectrum, we computed $\gamma_{810} = 0.01 \pm 0.03$, indicative of neither absorption nor emission. However, for the continuum-subtracted spectrum, we measured $\gamma_{810} = 1.6 \pm 0.4$. This combined with the similar characteristics of the silicate profile in M31 and M81, gives a much stronger indication that silicate emission is detected from M31*.

Measuring the radiated power from the M31 central engine can constrain the geometry and history of the emitting region. As discussed by Spinoglio et al. (1995), for both active and normal galaxies, the $12 \mu\text{m}$ luminosity is about 7% of the bolometric luminosity. With the important caveat that we are discussing only the nucleus, and not the entire galaxy, we can use the infrared spectrum to estimate the bolometric luminosity of the M31 nucleus. For the centre spectrum, we measure a $12 \mu\text{m}$ flux density of $0.062 \pm 0.002 \text{ Jy}$, which corresponds to a $12 \mu\text{m}$ luminosity of $(1.13 \pm 0.03) \times 10^{39} \text{ erg s}^{-1}$ and a bolometric luminosity of $(1.62 \pm 0.01) \times 10^{40} \text{ erg s}^{-1}$ ($\log L_{\text{bol}} = 40.21$). This

value is well within the range defined for low-luminosity AGN ($\log L_{\text{bol}} < 42$, Mason et al. 2012), and implies an Eddington ratio $L_{\text{bol}}/L_{\text{Edd}} \sim 10^{-7}$ for a black hole mass of $10^8 M_{\odot}$. Although the bolometric luminosity estimated from the mid-infrared is a factor of 10^3 times the bolometric luminosity estimated from the X-ray flux by Li et al. (2009), it certainly agrees with the general conclusion that the M31 nucleus radiates extremely inefficiently. A high infrared-to-X-ray ratio could indicate that the nucleus was brighter in the recent past and is now cooling; detailed modeling of the nucleus would require better constraints on the spectral energy distribution and is hence beyond the scope of this work.

Size of silicate emission region: $5\text{--}7''$, corresponding to $19\text{--}27 \text{ pc}$. "we can constrain the location of the silicate-emitting region to within 32 pc of the nucleus. This is the strongest constraint yet on the size of the silicate-emitting region in a Seyfert galaxy of any type." "To summarize, these observations permit us for the first time to set tight limits ($r \lesssim 32 \text{ pc}$) on the size of the silicate-emitting region in a Seyfert galaxy. This indicates that any silicate emission from the NLR must arise in its innermost regions. Alternatively, the silicate emission could come from the torus: we show that clumpy torus models give a reasonable fit to the silicate emission and the $220 \mu\text{m}$ SED, while at the same time obscuring the BLR. We emphasize that in the context of a clumpy torus the distinction of the transition from the outer torus to the inner NLR is more semantic than physical. Simultaneous modeling of emission lines and silicate emission from the NLR, as proposed by Schweitzer et al. (2008), may further illuminate the origin of the silicate emission features. Measurements on small spatial scales remain essential to identify the emitting structures in the cores of active galaxies." No fs lines present?

5 SUMMARY AND CONCLUSIONS

We obtained *Spitzer*/IRS spectral maps of 12 regions within M31 covering wavelengths $5\text{--}21 \mu\text{m}$. The spectra from those regions, except for the nucleus, are similar to spectra obtained from other nearby star-forming galaxies. Early ISO-CAM observations towards 4 regions of M31 showing a suppression of the $6\text{--}8 \mu\text{m}$ features and an enhancement of the $11.3 \mu\text{m}$ feature (Cesarsky et al. 1998) were likely affected by the background subtraction methods applied.

The PAH intensities in M31 regions show a decreasing trend with increasing radiation hardness, consistent with previous results from other nearby galaxies. The distribution of PAH EQWs with metallicity is well within the range of the starburst galaxy sample of Engelbracht et al. (2008). We did not have enough data from low-metallicity regions of M31 to observe the decreasing trend of EQWs at low metallicities which is visible in other galaxies.

Mid-infrared spectra from near the nucleus of M31 show either suppressed $6\text{--}8 \mu\text{m}$ features and a strong $11.3 \mu\text{m}$ feature ($15''$ off-nucleus) or silicate emission around $9.7 \mu\text{m}$ (on-nucleus). The nuclear spectrum is similar to that of six other nearby galaxies known to have low-luminosity AGN activity. This could strengthen the suggestion by Smith et al. (2007b) that low $L(7.7\mu\text{m})/L(11.3\mu\text{m})$ is an indicator of low luminosity AGN, but this feature ratio could also be due to a lack of ionized PAHs. The nuclear silicate emission is

another possible AGN indicator. The 12 μm luminosity can be used to estimate a bolometric luminosity for the M31 nucleus of $1.6 \times 10^{40} \text{ erg s}^{-1}$, well within the ‘low-luminosity’ classification, but well above the value estimated from the X-ray flux.

ACKNOWLEDGEMENTS

The authors thank D. Stock, K. Sandstrom and S. Lianou for fruitful discussions and technical support and S. Gallagher for helpful comments. We acknowledge support from NSERC Discovery Grants to PB and EP and an NSERC Discovery Accelerator Grant to EP. This work is based on observations made with the *Spitzer* Space Telescope, which is operated by the Jet Propulsion Laboratory, California Institute of Technology under a contract with NASA. This research has made use of NASA’s Astrophysics Data System. The version of the ISO data presented in this paper correspond to the Highly Processed Data Product (HPDP) set called ‘Mid-IR Spectro Imaging ISOCAM CVF Observations’ by Boulanger et al. (2005), available for public use in the ISO Data Archive.

REFERENCES

- Allamandola L. J., Tielens A. G. G. M., Barker J. R., 1989, *ApJS*, 71, 733
- Bacon R., Emsellem E., Combes F., Copin Y., Monnet G., Martin P., 2001, *A&A*, 371, 409
- Barmby P., et al., 2006, *ApJ*, 650, L45
- Beirão P., Brandl B. R., Devost D., Smith J. D., Hao L., Houck J. R., 2006, *ApJ*, 643, L1
- Bender R., et al., 2005, *ApJ*, 631, 280
- Boulanger F., et al., 2005, *A&A*, 436, 1151
- Brandl B. R., et al., 2006, *ApJ*, 653, 1129
- Calzetti D., et al., 2010, Conference Proceedings ‘Reionization to Exoplanets’, ed. P. Ogle, ASP Conference Series, Cesarsky C. J., et al., 1996, *A&A*, 315, L32
- Cesarsky D., Lequeux J., Pagani L., Ryter C., Loinard L., Sauvage M., 1998, *A&A*, 337, L35
- Croley M., Barmby P., Stock D., Azimlu M., Rosolowsky E., 2014, *MNRAS*, submitted
- Davidge T. J., Jensen J. B., Olsen K. A. G., 2006, *AJ*, 132, 521
- Devereux N., Ford H., Tsvetanov Z., Jacoby G., 2003, *AJ*, 125, 1226
- Diamond-Stanic A. M., Rieke G. H., 2010, *ApJ*, 724, 140
- Efstathiou A., Rowan-Robinson M., 1995, *MNRAS*, 273, 649
- Engelbracht C. W., Rieke G. H., Gordon K. D., Smith J.-D. T., Werner M. W., Moustakas J., Willmer C. N. A., Vanzi L., 2008, *ApJ*, 678, 804
- Galliano F., Madden S., Tielens A., Peeters E., Jones A., 2008a, *ApJ*, 679, 310
- Galliano F., Madden S. C., Tielens A. G. G. M., Peeters E., Jones A. P., 2008b, *ApJ*, 679, 310
- Garcia M. R., et al., 2010, *ApJ*, 710, 755
- Geballe T. R., Lacy J. H., Persson S. E., McGregor P. J., Soifer B. T., 1985, *ApJ*, 292, 500
- Gillett F. C., Forrest W. J., Merrill K. M., 1973, *ApJ*, 183, 87
- Gordon K. D., et al., 2006, *ApJ*, 638, L87
- Gordon K. D., Engelbracht C. W., Rieke G. H., Misselt K. A., Smith J.-D. T., Kennicutt Jr. R. C., 2008, *ApJ*, 682, 336
- Groves B., et al., 2012, *MNRAS*, 426, 892
- Hill A. R., Gallagher S. C., Deo R. P., Peeters E., Richards G. T., 2014, *MNRAS*, 438, 2317
- Hony S., Van Kerckhoven C., Peeters E., Tielens A. G. G. M., Hudgins D. M., Allamandola L. J., 2001, *A&A*, 370, 1030
- Houck J. R., et al., 2004, *ApJS*, 154, 18
- Hudgins D. M., Allamandola L. J., 2004, in Witt A. N., Clayton G. C., Draine B. T., eds, *Astronomical Society of the Pacific Conference Series Vol. 309, Astrophysics of Dust*, p. 665
- Kennicutt Jr. R. C., et al., 2003, *PASP*, 115, 928
- Kessler M. F., et al., 1996, *A&A*, 315, L27
- Kormendy J., 1988, *ApJ*, 335, 40
- Lauer T. R., et al., 1993, *AJ*, 106, 1436
- Li Z., Wang Q. D., Wakker B. P., 2009, *MNRAS*, 397, 148
- Li Z., Garcia M. R., Forman W. R., Jones C., Kraft R. P., Lal D. V., Murray S. S., Wang Q. D., 2011, *ApJ*, 728, L10
- Madden S. C., 2000, *New A Rev.*, 44, 249
- Mason R. E., Levenson N. A., Shi Y., Packham C., Gorjian V., Cleary K., Rhee J., Werner M., 2009, *ApJ*, 693, L136
- Mason R. E., et al., 2012, *AJ*, 144, 11
- McConnachie A. W., Irwin M. J., Ferguson A. M. N., Ibata R. A., Lewis G. F., Tanvir N., 2005, *MNRAS*, 356, 979
- Melchior A.-L., Combes F., 2013, *A&A*, 549, A27
- Moustakas J., Kennicutt Jr. R. C., Tremonti C. A., Dale D. A., Smith J.-D. T., Calzetti D., 2010, *ApJS*, 190, 233
- Muñoz-Mateos J. C., et al., 2009, *ApJ*, 703, 1569
- Nagao T., Maiolino R., Marconi A., 2006, *A&A*, 459, 85
- Netzer H., et al., 2007, *ApJ*, 666, 806
- Nowak N., Saglia R. P., Thomas J., Bender R., Davies R. I., Gebhardt K., 2008, *MNRAS*, 391, 1629
- Pagani L., Lequeux J., Cesarsky D., Milliard B., Lionard L., Sauvage M., 1999, *A&A*, 351, 447
- Peeters E., 2011, in *IAU Symposium*, pp 149–161, [arXiv:1111.3680](https://arxiv.org/abs/1111.3680), doi:10.1017/S174392131102494X
- Puget J. L., Leger A., 1989, *ARA&A*, 27, 161
- Roche P. F., Aitken D. K., Smith C. H., Ward M. J., 1991, *MNRAS*, 248, 606
- Sanders N. E., Caldwell N., McDowell J., Harding P., 2012, *ApJ*, 758, 133
- Sandstrom K. M., et al., 2012, *ApJ*, 744, 20
- Skillman E. D., Terlevich E., Terlevich R., 1998, *Space Sci. Rev.*, 84, 105
- Smith J.-D. T., et al., 2007a, *PASP*, 119, 1133
- Smith J.-D. T., et al., 2007b, *ApJ*, 656, 770
- Smith H. A., et al., 2010, *ApJ*, 716, 490
- Spinoglio L., Malkan M. A., 1992, *ApJ*, 399, 504
- Spinoglio L., Malkan M. A., Rush B., Carrasco L., Recillas-Cruz E., 1995, *ApJ*, 453, 616
- Spitzer Science Center 2012, *Spitzer Data Analysis Cookbook*, v5.0.1 edn. SSC, Pasadena, CA
- Spoon H. W. W., Marshall J. A., Houck J. R., Elitzur M., Hao L., Armus L., Brandl B. R., Charmandaris V., 2007, *ApJ*, 654, L49

Stock D. J., Peeters E., Tielens A. G. G. M., Otaguro J. N.,
Bik A., 2013, ApJ, 771, 72
Sturm E., et al., 2005, ApJ, 629, L21
Sturm E., et al., 2006, ApJ, 653, L13
Tielens A. G. G. M., 2008, ARA&A, 46, 289
Vermeij R., Peeters E., Tielens A. G. G. M., van der Hulst
J. M., 2002, A&A, 382, 1042
Werner M. W., et al., 2004, ApJS, 154, 1

This paper has been typeset from a \TeX / \LaTeX file prepared
by the author.